



HAL
open science

On the Reactivity of $\text{Li}_{8-y}\text{MnyP}_4$ toward Lithium

Frédéric Gillot, Laure Monconduit, Mathieu Morcrette, Marie-Liesse Doublet,
Loic Dupont, Jean-marie Tarascon

► **To cite this version:**

Frédéric Gillot, Laure Monconduit, Mathieu Morcrette, Marie-Liesse Doublet, Loic Dupont, et al..
On the Reactivity of $\text{Li}_{8-y}\text{MnyP}_4$ toward Lithium. *Chemistry of Materials*, 2005, 17, pp.3627-3635.
10.1021/cm050362b . hal-00383215

HAL Id: hal-00383215

<https://hal.science/hal-00383215>

Submitted on 12 May 2009

HAL is a multi-disciplinary open access archive for the deposit and dissemination of scientific research documents, whether they are published or not. The documents may come from teaching and research institutions in France or abroad, or from public or private research centers.

L'archive ouverte pluridisciplinaire **HAL**, est destinée au dépôt et à la diffusion de documents scientifiques de niveau recherche, publiés ou non, émanant des établissements d'enseignement et de recherche français ou étrangers, des laboratoires publics ou privés.

On the reactivity of $\text{Li}_{8-y}\text{Mn}_y\text{P}_4$ towards lithium

*F. Gillot*¹, *L. Monconduit*², *M. Morcrette*¹, *M-L. Doublet*³ and *J-M. Tarascon*¹

¹) LRCS -UMR 6007- Université de Picardie Jules Verne, 33 rue Saint-Leu, 80039 Amiens, France

²) LAMMI -UMR 5072 - Université Montpellier II, 2 Place Eugène Bataillon, 34095 Montpellier

³) LSDSMS -UMR 5636 - Université Montpellier II, 2 Place Eugène Bataillon, 34095 Montpellier

Abstract

The $\text{Li}_{5.5}\text{Mn}_{2.5}\text{P}_4$ and Li_7MnP_4 phases having a tetragonal structure ($a=b=4.176(1)$ Å and $c=5.978(1)$ Å) and a cubic structure ($a=5.968(3)$ Å), were synthesized by a two-step process consisting in ball milling Li, Mn and P powders followed by an annealing at 800°C under argon in a sealed stainless steel tube. The resulting materials were tested on Li cells between 0,01 and 2 V. Both of them can reversibly react with Li leading to reversible capacities as high as 1000 mAh/g, but only the $\text{Li}_{5.5}\text{Mn}_{2.5}\text{P}_4$ electrode can nicely maintain its initial capacity upon cycling. The origin of such a difference was found in the partial decomposition of Li_7MnP_4 in Li_3P and Mn nanoparticles at low potential, as deduced by *in situ* X-ray diffraction measurements. In contrast, no decomposition was shown to occur for the $\text{Li}_{5.5}\text{Mn}_{2.5}\text{P}_4$ electrode that shows the best capacity retention among all the ternary $\text{Li}_x\text{M}_y\text{P}_4$ (M= Ti, V) so far studied.

Corresponding author: frederic.gillot@sc.u-picardie.fr

Keywords: Lithium ion batteries, Manganese phosphides, Ball milling.

1. Introduction

In the search for new negative electrodes for Li-Ion batteries, various transition metal pnictides compounds (M-Pn; with Pn = N, Sb) have been recently studied, and promising electrochemical performances, namely in terms of gravimetric capacity ^[1-7] reported. Surprisingly, the pnictides phases with Pn = P have attracted less attention, although potentially more attractive in terms of gravimetric capacity, due to the lower atomic weight of phosphorus compared to antimony. Therefore, there are a few sparse reports on the electrochemical properties of binary compounds such as copper phosphide (CuP₂, Cu₃P), cobalt phosphide (CoP₃), manganese phosphide (MnP₄) and iron phosphide (FeP₂). It has been shown that the CuP₂,^[8] Cu₃P ^[9] and CoP₃ ^[10,11] systems can insert up to 3 Li per phosphorus atom leading to the formation of the Li₃P phase with metallic Cu or Co upon reduction (e.g. discharge). Upon recharge the reversibility of this displacement reaction was only demonstrated for the Cu₃P system. The FeP₂^[12] system was claimed to behave differently since the uptake of 6 Li during the first discharge leads to an amorphous metastable ternary “Li-Fe-P” phase without any evidence for metal extrusion.

Moving from binary to ternary P-based compounds, we investigated a new class of ternary phases having the Li₉TiP₄ ^[13] and Li₇VP₄ ^[13,14] compositions. When prepared by a two-step process, involving a mechanical grinding step prior to an annealing treatment at 800°C in a sealed stainless-steel vessel, both phases show a reversible uptake of 10 Li leading to capacities as high as 1000 mAh/g. This high number of exchanged Li was shown to provoke an amorphisation of the structure upon oxidation and its crystallization upon reduction resulting in poor capacity retention upon cycling. For such reasons, the mechanism, which leads to a repeated loss/reconstruction of the unit cell upon cycling, has been the subject of numerous studies. A mechanism nested in the M-P bond contraction/elongation of the tetrahedral (MP₄)^{x-} electronic entities constituting the building blocks of the precursor structure was put forward ^[15] to rationalize the amorphisation/recrystallization structural mechanism.

Owing to the recognized importance of the ionic-covalent character of the M-P bonds, with regard to the electrochemical performance of the ternary P-based compounds, we decided to extend our studies to Mn-based lithium phosphides by first revisiting the Li-Mn-P phase diagram earlier established by Juza et al. ^[16] in the 60s. By annealing at temperatures between 600°C and 800°C in evacuated sealed silica tubes mixture of elements (or Li₃P + Mn + P), the authors were able to isolate several phases of the ternary Li-Mn-P system, obeying

the general formula $\text{Li}_{8-y}\text{Mn}_y\text{P}_4$ for y varying between 1 and 4. Over the identified compounds, there were the Li_7MnP_4 and $\text{Li}_{6.6}\text{Mn}_{1.3}\text{P}_4$ (referred to as Li_5MnP_3) phases having a cubic structure, and the $\text{Li}_6\text{Mn}_2\text{P}_4$ (Li_3MnP_2), $\text{Li}_4\text{Mn}_4\text{P}_4$ (LiMnP) and $\text{Li}_{5.5}\text{Mn}_{2.5}\text{P}_4$ phases having a tetragonal structure. For sake of comparison, Li_7MnP_4 and $\text{Li}_{5.5}\text{Mn}_{2.5}\text{P}_4$ crystal structures are shown as inserts in **Fig. 1** and **2**, respectively. Li_7MnP_4 crystallizes in the Fm-3m space group in which the phosphorus atoms sit in the 4a (0,0,0) sites forming a *fcc* network, and the manganese and lithium metal cations are statistically distributed over the 8c ($\frac{1}{4}, \frac{1}{4}, \frac{1}{4}$) tetrahedral sites. In contrast, $\text{Li}_{5.5}\text{Mn}_{2.5}\text{P}_4$ crystallizes in the space group $\text{P } 4/n \text{ m m}$, in which all the manganese cations are localized in the same site (2b) thus forming planes of corner-shared regular MnP_4 tetrahedral perpendicular to the c axis. This ordering between Li and Mn induces a distortion that confers to the structure a layered organization (Inset of **Fig. 2**). In $\text{Li}_6\text{Mn}_2\text{P}_4$, this 2b site consists of mixed half Mn and Li. The “ MnP_4 ” tetrahedral entities are no longer isolated as in Li_7MnP_4 , but form chains or incomplete layers running perpendicular to the c -axis. This type of layer would become complete when the composition in manganese equals 4 as observed for the $\text{Li}_4\text{Mn}_4\text{P}_4$ phase.

The main drawback of the early study ^[16] of the $\text{Li}_{8-y}\text{Mn}_y\text{P}_4$ phase diagram resides in the preparation of single-phased materials owing to the close structures and high stabilities of the competing binary Mn-P phases, hence to the difficulty in precisely determining their electrochemical signature or probing their electrochemical performances vs. Li. To bypass this issue we have successfully extended, as reported herein, our well established synthesis protocol of the Li_9TiP_4 and Li_7VP_4 compounds to the elaboration of $\text{Li}_{8-y}\text{Mn}_y\text{P}_4$ single-phased materials. For reasons of conciseness, only the synthesis, electrochemical properties and lithium reactivity mechanisms of the cubic Li_7MnP_4 ($y=1$) and tetragonal $\text{Li}_{5.5}\text{Mn}_{2.5}\text{P}_4$ ($y=2.5$) phases with respect to lithium are investigated in this paper.

2. Results

a) Synthesis

Based on our recent work on Li_9TiP_4 ,^[13, 14, 17] the ball milling synthesis approach was used to survey the $\text{Li}_{8-y}\text{Mn}_y\text{P}_4$ phase diagram with special attention to the Li_7MnP_4 and $\text{Li}_{5.5}\text{Mn}_{2.5}\text{P}_4$ phases. Within argon dry-box, raw powders of Mn, P and Li elements were first mixed in the right stoichiometry to form the selected $\text{Li}_{8-y}\text{Mn}_y\text{P}_4$ phases ($y=1$; $y=2.5$). The mixed powders were then placed into a stainless steel container together with steel balls in a one to ten weight ratio. Once hermetically closed, the container was placed onto a Spex 8000

mixer-mill that generates mechanical strains. Milling times of 50 hours were found to be sufficient to produce poorly crystallized powders showing, as deduced by X-rays, the main (111), (220) and (001), (101), (111), (112), (200) Bragg peaks of the Li_7MnP_4 and $\text{Li}_{5.5}\text{Mn}_{2.5}\text{P}_4$ phases, respectively. Owing to the experimental observations that longer milling treatments did not improve the powder crystallinity, the milled powders were placed in a sealed stainless steel tube, and annealed at 800°C for about one week. Afterwards, the recovered powders were characterized for their structure, texture and composition.

X-ray diffraction studies did indicate that both samples of nominal composition “ Li_7MnP_4 ” (**Fig. 1**) and “ $\text{Li}_{5.5}\text{Mn}_{2.5}\text{P}_4$ ” (**Fig. 2**) were well-crystallized, and devoid of any impurity phases since all the Bragg peaks appearing in their X-ray powder patterns could be indexed (**Fig. 1**) on the basis of a cubic structure with $a=5.968\text{\AA}$ or (**Fig. 2**) a tetragonal unit cell with $a=b=4.176(1)\text{\AA}$ and $c=5.978(1)\text{\AA}$. The measured lattice parameters nearly coincide with those reported in the literature ^[16] for Li_7MnP_4 ($a=5.977\text{\AA}$) and $\text{Li}_6\text{Mn}_2\text{P}_4$ ($a=b=4.164\text{\AA}$ and $c=5.983\text{\AA}$). We thus assume the $\text{Li}_{5.5}\text{Mn}_{2.5}\text{P}_4$ phase to crystallize in the same space group as $\text{Li}_6\text{Mn}_2\text{P}_4$ with the slight differences in lattice parameters being simply nested in the small deviation of the lithium and manganese contents compared to the literature. The comparison between the two diagrams emphasizes two important features. First, in $\text{Li}_{5.5}\text{Mn}_{2.5}\text{P}_4$, we do not have a *fcc* structure due to Mn and Li ordering, this implies a difference in the space group moving from a F character for Li_7MnP_4 to a P character for $\text{Li}_{5.5}\text{Mn}_{2.5}\text{P}_4$. As a consequence, two important peaks located around $2\theta \cong 17^\circ$ and 39° , appear in $\text{Li}_{5.5}\text{Mn}_{2.5}\text{P}_4$ diagram. Moreover, the cubic network is lost as it can be observed in the splitting of the (200) peak in the $\text{Li}_{5.5}\text{Mn}_{2.5}\text{P}_4$ diagram.

The Li_7MnP_4 and $\text{Li}_{5.5}\text{Mn}_{2.5}\text{P}_4$ samples were further studied by scanning electron microscopy (SEM) coupled with an energy dispersive X-ray analyser (EDX). The $\text{Li}_{5.5}\text{Mn}_{2.5}\text{P}_4$ sample consists of micron-sized particles forming agglomerates exceeding $10\mu\text{m}$ in diameter (**Fig. 3**), and having Mn to P atomic ratio of 0.61, which nearly fits the nominal value of 0.625. Similar agreement between experimental and nominal compositions is found for the Li_7MnP_4 powders with apparently larger primary particles leading then to a less divided sample than the $\text{Li}_{5.5}\text{Mn}_{2.5}\text{P}_4$ one.

b) Electrochemical properties

The synthesized $\text{Li}_{5.5}\text{Mn}_{2.5}\text{P}_4$ and Li_7MnP_4 powders were tested for their electrochemical performances vs. Li in SwagelokTM-type cells assembled in an argon-filled dry box, with oxygen and water contents below 5 ppm. The cells consist of a composite positive electrode, containing 10-12 mg of active material mixed with 15 % of carbon sp, parted from the negative Li electrode foil by a WhatmanTM-GF/D borosilicate glass micro-fiber separator, saturated with a LP 30 (LiPF_6 (1M) in EC:DMC (1:1)) electrolyte solution. Electrochemical uptake/removal of Li was monitored using a VMP automatic cycling data recording system (Biologic SA, Claix, France) operating in a galvanostatic mode.

Owing to the large initial Li content in the precursor phase, the measurements were started on charge with a resting initial potential of 1.17 V and 1.3 V for the $\text{Li}_7\text{MnP}_4/\text{Li}$ and $\text{Li}_{5.5}\text{Mn}_{2.5}\text{P}_4/\text{Li}$ cells, respectively. The potential vs. composition curves for the two cells charged up to 2 volts are shown in **Fig. 4** and **5**. Once the first charge is achieved, both electrodes can uptake on discharge large amounts of lithium (Δx) per formula unit leading to capacities as high as 1000 mAh/g for Li_7MnP_4 ($\Delta x=9$) and 900 mAh/g for $\text{Li}_{5.5}\text{Mn}_{2.5}\text{P}_4$ ($\Delta x=8$). However, this initial apparent similarity no longer holds upon subsequent cycling since the $\text{Li}_7\text{MnP}_4/\text{Li}$ cell shows a 21% and 58% capacity loss after the second and third charge, whereas the $\text{Li}_{5.5}\text{Mn}_{2.5}\text{P}_4/\text{Li}$ cell shows only a 10% capacity fading after 25 cycles, respectively. Besides, we note that the cycling performance of the $\text{Li}_7\text{MnP}_4/\text{Li}$ cell can be improved (**Fig. 6**) to the expense of a capacity penalty (500 mAh/g instead of 1000 mAh/g) by narrowing the cycling voltage (0.5 V to 1.7 V instead of 0.01 to 2 V). This is indicative of the poor reversibility of the Li uptake/removal process occurring below 0.5 V for the Li_7MnP_4 electrode as compared to the $\text{Li}_{5.5}\text{Mn}_{2.5}\text{P}_4$ one. To gain further insight into the origin of these differences, *in situ* X-ray diffraction and high-resolution electron microscopy studies were pursued in parallel.

c) In situ X-Ray Diffraction (XRD)

To determine any structural modification induced by Li uptake/removal, *in situ* XRD experiments were performed upon cycling on a $\text{Li}_{8-y}\text{M}_y\text{P}_4/\text{Li}$ cells, by means of a D8 Brucker X-ray diffractometer with $\text{CoK}\alpha$ radiation. The *in situ* electrochemical cell was mounted in a dry box as reported before ^[19] by placing the studied electrode material underneath a beryllium window used as current collector, the rest of the electrochemical active part of the cell remains the same as in our Swagelok configuration. The complete device is then placed in the diffractometer and connected to the VMP cycling system.

We present the data for a $\text{Li}_{5.5-x}\text{Mn}_{2.5}\text{P}_4/\text{Li}$ cell but let's first recall for sake of clarity that we can distinguish the cubic phase from the tetragonal one by spotting the position of the (111) Bragg peaks and more specifically the shape of the (200) Bragg peak that is split for the tetragonal phase. Full pattern matching of the different X-rays recorded upon charge and discharge were carefully analysed in order to see the presence of a cubic \rightarrow tetragonal phase transition. Furthermore, we should bear in mind that in such cubic system, the disappearance of (001) and (201) peaks is the proof of a new phase having a cubic face centred unit cell, and not indicative of a tetragonal distortion.

As the cell is charged (e.g. removal of Li) the intensity of the Bragg peaks starts decreasing. This decrease is concomitant with slight shifts of the (101) and (112) Bragg peaks towards lower 2θ angles, (**Fig. 7a**) suggesting an decrease in the lattice parameters and consequently in the unit cell volume. Note that upon pursuing further the charging process up to $x=4.5$, " $\text{Li}_1\text{Mn}_{2.5}\text{P}_4$ ", there is a total disappearance of the (001) and (111) Bragg peaks, while the (200) Bragg peak can still be nicely observed (**Fig. 7a** bottom). Based on such an observation, it will be tempting to claim that the removal of Li from $\text{Li}_{5.5-x}\text{Mn}_{2.5}\text{P}_4$, which involves a change in the unit cell symmetry, occurs through a two-phase rather than a single phase process, with the end member phase " $\text{Li}_1\text{Mn}_{2.5}\text{P}_4$ " having a cubic-type symmetry. However, caution has to be exercised owing to the barely detectable intensity of these peaks at the end of the charge that prevents any reliable structural information on the fully electrode delithiated phase.

In the latter case, by ascribing the single peak to a (220) Bragg reflection in the cubic space group, we will show a difference in volume between the beginning and the end of charge of about 5%. However, owing to the poor resolution of the collected X-ray powder patterns together with the limited amount of Bragg peaks considered further neutron experiment studies have been performed.

The X-ray powder patterns collected during the reduction of the $\text{Li}_1\text{Mn}_{2.5}\text{P}_4$ indicate a reversible process since the Bragg peaks corresponding to the tetragonal $\text{Li}_{5.5-x}\text{Mn}_{2.5}\text{P}_4$ phase progressively re-appear (**Fig. 7b**) to become the most intense for $x=0$. At that composition, $\text{Li}_{5.5}\text{Mn}_{2.5}\text{P}_4$ has regained its well-crystallized structure with however smaller lattice parameters ($a=b=4.157(5)$ Å, $c=5.968(2)$ Å) compared to the initial phase ($a=b=4.176(1)$ Å and $c=5.978(1)$ Å). The origin of such differences is most likely nested in our uncertainties in precisely controlling the x values.

Additional lithium (about 4 per unit cell) can be inserted into $\text{Li}_{5.5}\text{Mn}_{2.5}\text{P}_4$ below 0.4 V (**Fig. 5**) implying structural modifications with the possibility of occupying the four octahedral empty sites marked on the figure 2 inset. This is consistent with the *in situ* XRD data, which shows that the insertion of Li into the electrochemically recovered “ $\text{Li}_{5.5}\text{Mn}_{2.5}\text{P}_4$ ” phase (**Fig. 7b**) results in a continuous shift of its tetragonal Bragg peaks towards low 2θ angles (e.g. increase in the lattice parameters) together with a progressive disappearance of the 001 and 201 peaks. Such peaks have completely vanished when the value of x reaches 3 (e.g. “ $\text{Li}_{8.5}\text{Mn}_{2.5}\text{P}_4$ ”) suggesting that we have switched from a tetragonal P 4/n m m space group to a cubic F m $\bar{3}$ m one having lattice parameters very close to those of the tetragonal one, so that such structural transition solely results in a 2% volume change. This transformation is quite surprising since it implies that Li and Mn are statistically distributed in all the tetrahedral sites of the cubic-faced centred array of phosphorus. Such a Li-driven displacement does not come too much as a surprise since already reported on spinel-type compounds (LiMn_2O_4)^[20] or on layer chalcogenides (NiPS_3)^[21] upon Li-reduction.

The electrochemical addition of more Li-ions into this phase, by lowering the cell discharge voltage to 0.01 V does solely induce a shift of the Bragg peaks to lower angles, and enables the formation of a phase having the $\text{Li}_{9.5}\text{Mn}_{2.5}\text{P}_4$ stoichiometry ($a=6.032(4)$ Å) (**Fig. 7b**). Interestingly, the total unit cell volume variation of the fully charged “ $\text{Li}_{1.5}\text{Mn}_{2.5}\text{P}_4$ ” and discharged compounds “ $\text{Li}_{9.5}\text{Mn}_{2.5}\text{P}_4$ ” remains less than 4%.

The electrochemical *in situ* X-ray cell was monitored over subsequent cycles, and the X-ray powder patterns collected as above. An analysis of these XRD powder patterns, not shown here because identical to the sequences presented in **Fig. 7a** and **7b**, did clearly indicate that all of the processes (e.g. phases changes) observed during the first charge and discharge were fully reversible. For instance, the X-ray powder patterns of the electrode phase obtained at the end of the second and tenth charges were found to perfectly superimpose with the one obtained at the end of the first cycle. This is totally consistent with the aptitude of this compound to sustain its reversible electrochemical capacity when cycled vs. Li as previously shown.

In order to understand the difference between the electrochemical properties (higher capacity retention for $\text{Li}_{5.5}\text{Mn}_{2.5}\text{P}_4$ electrode) when the manganese content increases, an *in situ* X-ray diffraction $\text{Li}_7\text{MnP}_4/\text{Li}$ cell was assembled and charged up to 2 V prior to be fully discharged down to 0.01 V. Upon Li removal (**Fig. 8a**) there is a progressive shift of the (111) and (220) towards higher 2θ angles parallel to a decrease in the peak intensity. For x values reaching 2, the X-ray powder patterns become featureless, indicative of a total

amorphous phase at least with respect to x-rays, and remains the same up to the end of the delithiation process. The fully charged phase of composition “ $\text{Li}_{1.3}\text{MnP}_4$ ” is amorphous in contrast to the fully charged “ $\text{Li}_{1.5}\text{Mn}_{2.5}\text{P}_4$ ” phases that were still barely crystallized. The electrochemical lithiation of the fully oxidized “ $\text{Li}_{1.3}\text{MnP}_4$ ” phase (**Fig. 8b**) leads to an evolution of its X-ray powder patterns with the re-appearance, for x values approaching 4, of the (111) and (220) Bragg peaks corresponding to the cubic phase that continuously grows until composition close to $x=7.3$, indicative that the material has converted back to its initial well-crystallized structure. Thus, the Li removal/uptake process in Li_7MnP_4 linked to an amorphisation/crystallization of the electrode material appears perfectly reversible. Further pursuing the electrochemical lithiation of the Li_7MnP_4 phase by lowering the cell voltage down to 0.01 V results in a progressive decrease in intensity of the (111) and (220) Bragg peaks together with the progressive appearance of two extra Bragg peaks located at $2\theta = 31^\circ$ and 50° corresponding to the formation of Li_3P . Such a low voltage decomposition reaction could be at the origin of the poor cycling performance of the Li_7MnP_4 phase. This hypothesis is further supported by the ability to improve the cycling performance of this phase by lowering the cell cut-off voltage (e.g. by staying out of this phase decomposition domain) as previously shown. Now the obvious question is whether such a decomposition reaction bears some similarity to our previously reported conversion reactions, and therefore leads to the formation of metallic particles. To answer such a question high-resolution electron microscopy measurements were performed.

d) High Resonance Transmission Electronic Microscopy (HRTEM)

A $\text{Li}_7\text{MnP}_4/\text{Li}$ Swagelok cell was charged up to 2V then discharged down to 0.01V prior to being disassembled in a glove box to recover the cycled powder, which was then washed with pure DMC to remove electrolyte traces. The textural/micro structural characterization study was performed by means of a TECNAI F20 microscope fitted with EDAX EDS analysis, and equipped with in-house-designed sample holders enabling investigations of moisture-sensitive samples without any air exposure. Recorded SAED pattern were processed with the Process Diffraction^[18] software in order to obtain an X-ray like diffraction pattern (Intensity versus 2θ (λ_{Co})).

The electrode is made of large dark "particles" (5 to 10 μm wide) presenting a grey contrast on the edge (**Fig. 9a**). Two hypotheses could be proposed to explain such a contrast difference: the "particles" have a thick heart and thin edges or the "particles" are surrounded

by an important layer, often observed on numerous materials discharged down to 0.01V, due to the decomposition of the electrolyte by metallic nanoparticles formed during the reduction. It was previously reported that this layer vanished under an intense electron beam. This phenomenon could be nicely observed on the overall (**Fig. 9a**) and enlarged (**Fig. 9c**) images where a deep beam impact and a huddling of the layer are observed, and noted by a white arrow on the **Fig. 9**, respectively. The use of the electron beam to destroy the polymeric layer allows to visualize the true nature of the "particles" and specifically the nanoparticles inducing the electrolyte decomposition (**Fig. 9c**). These nanoparticles are packed together in such a way that it is very difficult to distinguish the outlines of one of them. The average diameter size is estimated between 20 and 100Å. In order to determine the nature of the phases implicated by the formation of nanograins, a Selected Area Electron Diffraction (SAED) pattern was recorded then processed with Process diffraction software. The so-obtained X-ray like diffraction pattern (**Fig. 9b**) could be indexed using calculated Li_3P (lozenge mark) and metallic manganese (circle mark) reflections. This indexing is perfectly consistent with a decomposition reaction occurring during the discharge with the formation of manganese nanoparticles embedded in Li_3P matrix. The punctual EDS analysis (**Fig. 10**) realized on agglomerates confirms this assertion. Using a very small electron probe (less than 100Å), the Li_3P matrix could be isolated on the edge of the agglomerate inducing only the phosphorus signal on the EDS window (**Fig. 10a**) while both phosphorus and manganese signal are observed on the same windows (**Fig. 10b**) as soon as the electron beam is moved to the agglomerate centre.

Such a decomposition reaction leading to the formation of Li_3P and Mn nanoparticles bears some similarities to our recently reported work dealing with the electrochemically reactivity of 3d-metal binary oxides towards Li through a novel process termed "conversion reaction" that entails at low potential the formation of metal nanoparticles embedded in a Li_2O matrix. This comparison will tend to naively imply that the observed decomposition reaction observed with Li_7MnP_4 should not penalize its capacity retention. We believe it is not so because of the existence of other decomposition products that we could not detect by HREM. Such a belief is based on our own experience with ternary borates electrodes and on the observation that, although these materials react with Li through conversion reactions, they could not sustain their attractive initial capacity upon cycling owing to, besides the growth of Li_2O and metal nanoparticles at low potential, the formation of another electrochemically inactive Li_3BO_3 phase solely identified by NMR.

3. Discussion

We have studied the electrochemical reactivity of two members ($\text{Li}_{5.5}\text{Mn}_{2.5}\text{P}_4$ and Li_7MnP_4) of the $\text{Li}_{8-y}\text{Mn}_y\text{P}_4$ phase diagram towards Li, over a wide range of potential. By means of *in situ* X-ray diffraction and HRTEM measurements we have shown that both materials react differently. For the quadratic $\text{Li}_{5.5}\text{Mn}_{2.5}\text{P}_4$ phase that shows an excellent cyclability vs. Li, the Li uptake/removal processes occur through smooth evolution of lattice parameters while preserving the crystalline nature of the material. This is different for the cubic Li_7MnP_4 phase for which Li-uptake/removal processes were associated with an amorphisation/crystallization mechanism, probably accompanied with some kind of irreversible decomposition at the end of discharge, leading to a poor electrode cycling life.

For sake of comparison we recall that the electrochemical reactivity vs. Li of other Li-based ternary phosphorous compounds such as Li_7VP_4 and Li_9TiP_4 has been previously studied. Both phases crystallize in a cubic structure and similarly react with a large amount of Li and poor capacity retention, as for Li_7MnP_4 . Like for Li_7MnP_4 the uptake/removal of Li in Li_9TiP_4 was associated with an amorphisation /crystallization process but no evidence for phase decomposition was observed at low potential, in contrast to Li_7MnP_4 . Then phase decomposition cannot solely explain the rapid capacity fading. From a direct observation that all cubic phases (Li_7VP_4 , Li_9TiP_4 and Li_7MnP_4) exhibit poor cycling performances in contrast to tetragonal phases ($\text{Li}_{5.5}\text{Mn}_{2.5}\text{P}_4$), one could conclude that the crystal structure plays a key role in governing the cycling life of these electrodes. Actually, we believe that more than the crystal structure, the heavy metals stoichiometry is likely to be responsible for the electrode performances. Indeed, the tetragonal structure can be easily deduced from the cubic one, as soon as more than one transition metal occurs in the unit cell. The three different Mn-Mn interactions that one can generate by ordering two manganese atoms in the 8c tetrahedral sites of the cubic cell give raise to three different networks, as shown **Fig. 11**. These networks describe chains of edge-shared MnP_4 tetrahedral (A), and two-dimensional or three-dimensional lattices of corner-shared MnP_4 tetrahedral (B and C). A comparison between these structures and the tetragonal structure of $\text{Li}_6\text{Mn}_2\text{P}_4$ or $\text{Li}_{5.5}\text{Mn}_{2.5}\text{P}_4$ obviously stresses the B-type structure as the most favourable structure for $\text{Li}_{8-y}\text{Mn}_y\text{P}_4$ with $y > 1$. This is supported by a molecular orbital analysis that shows a greater stability of the Mn 3d-orbitals when the two MnP_4 tetrahedra are connected through one P bridge (corner-sharing) instead of two P

bridges (edge-sharing). For $\text{Li}_6\text{Mn}_2\text{P}_4$, the metallic formal oxidation state leads to the d^4 electron count, *i.e.* to the filling of the two-degenerated e -type orbitals of the MnP_4 tetrahedron, the t_2 -type orbitals lying higher in energy. As shown by the crystal orbital overlap population (COOP) analysis (**Fig. 12**), the e -type band lying just below the Fermi level is characterized by strong bonding P-P levels and strong anti-bonding Mn-P levels. This may explain the slight distortion of the tetragonal lattice compared to the cubic one, as the P-P levels do not occur in the Li_7MnP_4 electronic band structure, whereas equivalent Mn-P anti-bonding levels do. Upon charge, the removal of electrons from these P-P bonding states is thus expected to induce an increase in the P-P distance, and therefore a slight increase in the a - and b -lattice parameters back to the cubic cell. Upon discharge, the filling of the anti-bonding Mn-P levels lying just above the Fermi level of the $\text{Li}_6\text{Mn}_2\text{P}_4$ electronic structure induces an increase in the Mn-P distances, once again yielding a tetragonal to cubic distortion. Between these two extreme fillings, it is probable that Mn-Mn magnetic interactions could also contribute to the tetragonal structure stabilization, as local magnetic moments should occur on the manganese cations. Work is in progress to get more insight into these possible magnetic interactions.

This work then underlies the importance of changing 1) the nature of the 3d metal cation (from Ti to V or Mn), 2) the 3d-metal cation content (from 1 to 2.5 per formula unit), and 3) the nature of the ligand with respect to the electronic band structure of these materials and in retrospective to their crystal structures. Along that line it does not come as a surprise that a mechanism nested in the M-P bond contraction/elongation of the tetrahedral $(\text{MP}_4)^{x-}$ electronic entities constituting the building blocks of the precursor structure was put forward ^[15] to account for the loss/reconstruction of the unit cell previously observed within the Li_9TiP_4 phase. To provide more solid ground to the above speculations, we have undertaken a collaborative work in order to extend the electronic calculations previously done on Li_9TiP_4 to the Li_7MnP_4 and $\text{Li}_{5.5}\text{Mn}_{2.5}\text{P}_4$ phases, and to confront these results with XANES and EELS measurements presently in progress.

Conclusion

Through the study of the Li-Mn-P system, we have prepared a phase $\text{Li}_{5.5}\text{Mn}_{2.5}\text{P}_4$ that presents the best cycling performance ever reported so far for any Li-based 3d metal phosphorus systems. The uniqueness of this compound was ascribed to its tetragonal crystal structure although we are lacking of electronic calculations to ground such a statement. Presently, besides conducting electronic calculations, our work aims at confirming, through *in situ* XANES measurements, that redox chemistry in transition metal pnictides involves stable $(\text{MPn}_4)^{\delta-}$ anionic entities able to accommodate large charge variations. Furthermore, in light of such findings we are revisiting the electrochemical performance of various phosphorus systems, either ternary or binary, by playing both on the nature of the 3d metal and on the 3d-metal/P ratio.

References

- (1.) M. Nishijima, T. Kagohashi, M. Imanishi, Y. Takeda, O. Yamamoto, S. Kondo, *Solids State Ionics*, **83** (1996) 107.
- (2.) T. Shodai, Y. Sakurai, T. Suzuki, *Solids State Ionics*, **122** (1999) 85.
- (3.) R. Alcantara, F.J. Fernandez-Madrigo, P. Lavela, J.L. Tirado, J-C. Jumas, J-O. Fourcade, *J. Mater. Chem.*, **9** (1999) 2517.
- (4.) F.J. Fernandez-Madrigo, P. Lavela, C.P. Vicente, J.L. Tirado, *J. Electroanal. Chem.*, **501** (2001) 205.
- (5.) Y. Takeda et al, *Solids State Ionics*, **130** (2000) 61.
- (6.) J.L.C. Rowsell, V. Pralong, L.F. Nazar, *J. Am. Chem. Soc.*, **123** (2001) 8598.
- (7.) H. Honda, H. Sakaguchi, I. Tanaka, T. Esaka, *J. Power Sources.*, **123** (2003) 216.
- (8.) K. Wang, J. Yang, J. Xie, B. Wang, Z. Wen, *Electrochem. Commun.*, **5** (2003) 480.
- (9.) H. Pfeiffer, F. Tancret, M.P. Bichat, L. Monconduit, F. Favier, T. Brousse, *Electrochem. Commun.*, **6** (2004) 263.
- (10.) R. Alcantara, J.L. Tirado, J-C. Jumas, L. Monconduit, J. Olivier Fourcade, *J. Power Sources.*, **109** (2002) 308.
- (11.) V. Pralong, D.C.S. Souza, K.T. Leung, L.F. Nazar, *Electrochem. Commun.*, **4** (2002) 516.
- (12.) D.C.C. Silva, O. Crosnier, G. Ouvrard, J. Greedan, A. Safa-Sefat, L.F. Nazar, *Electrochemical and Solid-State Letters*, **6**(8) (2003) A162.
- (13.) M.-L. Doublet*, F. Lemoigno, M.-P. Bichat, F. Favier*, L. Monconduit
Proceedings of the 204th Meeting of the Electrochem. Soc. PV-2003-19 (2004)
- (14.) F. Gillot, M.P. Bichat, F. Favier, M. Morcrette, M.L. Doublet, L. Monconduit, *Electrochimica Acta*, **49**(14) (2004) 2325.

- (15.) M.P. Bichat, F. Gillot, L. Monconduit F. Favier, M. Morcrette, F. Lemoigno, M.L. Doublet, *Chem. Mater.*, **16** (2004) 1002. F. Gillot, Ph.D. Thesis, Montpellier II University (2003).
- (16.) R. Juza and T. Bohman, *Z. Anorg. Allg. Chem.*, **308** (1961) 159.
- (17.) M. Morcrette, F. Gillot, L. Monconduit, J-M. Tarascon, *Electrochem. Solid-State Lett.*, **A59** (2003) 6.
- (18.) S. Suzuki, T. Sshodai, *Solids State Ionics*, **116** (1999) 1-9.
- (19.) M. Morcrette, Y. Chabre, G. Vaughan, G. Amatucci, J-B. Leriche, S. Patoux, C. Masquelier, J-M. Tarascon, *Electrochimica Acta*, **47** (2002) 3137.(20.) L. Dupont, M. Hervieu, G. Rouse, C. Masquelier, M. R. Palacin, Y. Chabre, J.M. Tarascon, *J. Solid State Chem.*, **155** (2000) 394-408.
- (21.) R. Brec, E. Prouzet and G. Ouvrard, *J. Power Sources*, **43-44** (1993) 277-288.
- (22.) S. C. Lai, *J. Electrochem. Soc.*, **123** (1976) 1196. R. A. Sharma and R. N. Seefuth, *J. Electrochem. Soc.*, **123** (1976) 1763.
- (23.) J.O. Besenhard, J. Yang, M. Winter, *J. Power Sources*, **68** (1997) 87.

Figure Captions

- Figure 1: X-Ray diffraction pattern of Li_7MnP_4 and its refinement obtained by full pattern matching using Winplot Software.
- Figure 2: X-Ray diffraction pattern of $\text{Li}_{5.5}\text{Mn}_{2.5}\text{P}_4$ and its refinement obtained by full pattern matching using Winplot Software.
- Figure 3: SEM images of a) Li_7MnP_4 and b) $\text{Li}_{5.5}\text{Mn}_{2.5}\text{P}_4$. Both compounds are made of micron-sized particles
- Figure 4: Voltage vs. composition curve of Li_7MnP_4 between 2 and 0.01 V recorded with a scan rate of 1Li / 20h together with its capacity retention showed in insert.
- Figure 5: Voltage vs. composition curve of $\text{Li}_{5.5}\text{Mn}_{2.5}\text{P}_4$ between 2 and 0.01 V recorded with a scan rate of 1Li / 2h together with its capacity retention showed in insert.
- Figure 6: Voltage vs. composition curve of Li_7MnP_4 with a different voltage window (between 1.7 and 0.5 V) recorded with a scan rate of 1Li / 2h. Note the improvement of the capacity retention (showed in insert) compared to the Fig. 4.
- Figure 7: *In situ* X-Ray diffraction pattern of $\text{Li}_{5.5-x}\text{Mn}_{2.5}\text{P}_4$ / Li cell recorded at different stages of the charge (a) and discharge (b).
- Figure 8: *In situ* X-Ray diffraction pattern of $\text{Li}_{7-x}\text{MnP}_4$ /Li cell recorded at different stages of the charge (a) and discharge (b).
- Figure 9: a) Overall TEM image realized on charged then discharged Li_7MnP_4 phase. b) Corresponding SAED pattern (offset) processed in order to obtain X-ray like diagram. c) Enlarged TEM image showing nanoparticles as well as polymeric coating. The white arrows refer to the vanishing of this coating under the electron

Beam. The lozenge and circle marks note the theoretical Li_3P and Manganese peak positions, respectively

Figure 10: a) and b) EDS spectra recorded, between 1 and 7 keV using a small electron probe ($<100\text{\AA}$), on the edge and near the centre of an agglomerate reported on c)

Figure 11 : Three networks deduced from the different arrangements of two Mn in the 8c tetrahedral sites of the *f.c.c.* P-based network.

Figure 12 : Crystal Orbital Overlap Population (COOP) calculated for the Mn-P (red) and the P-P (blue) bonds in $\text{Li}_6\text{Mn}_2\text{P}_4$. EF stands for the Fermi level.

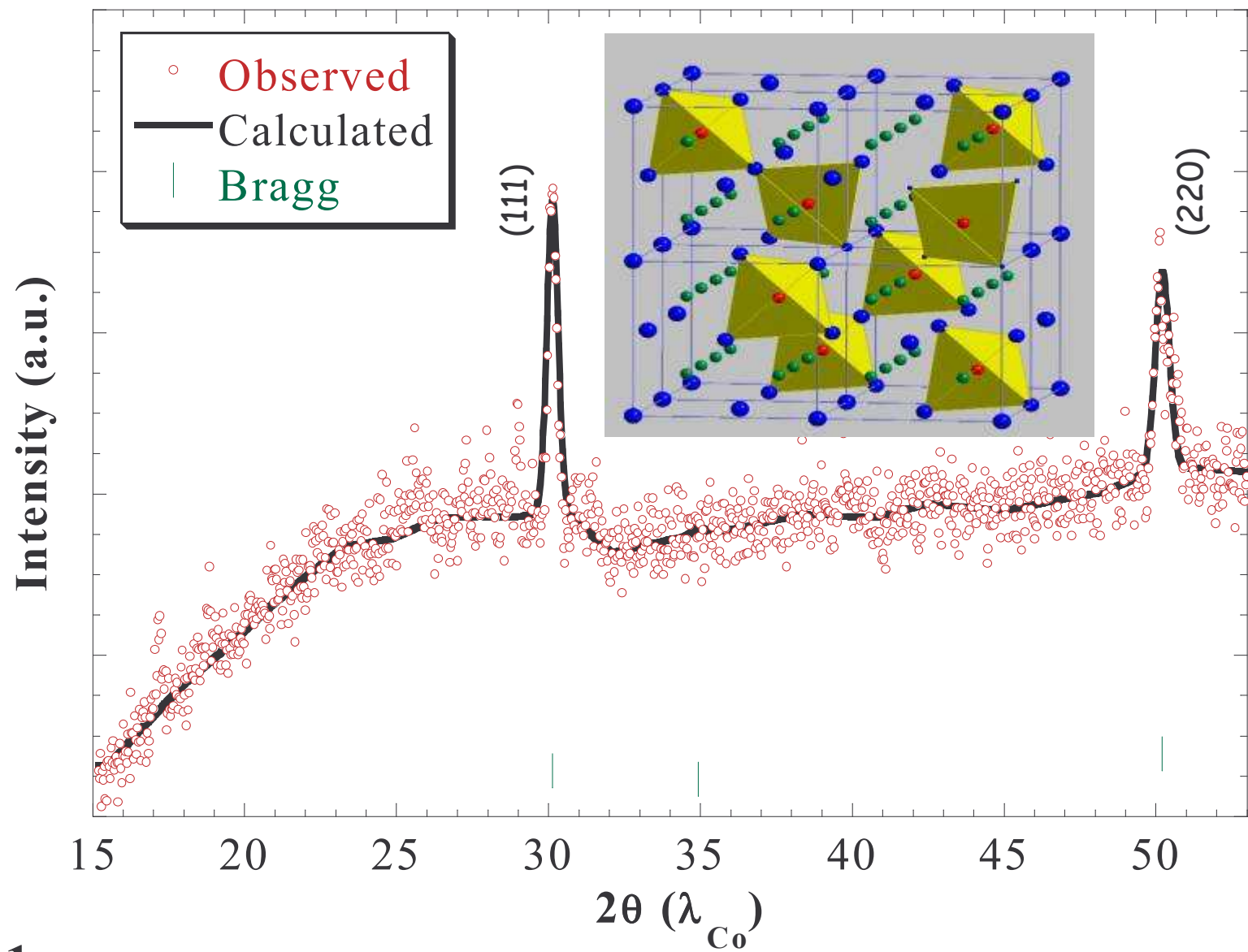


Fig. 1

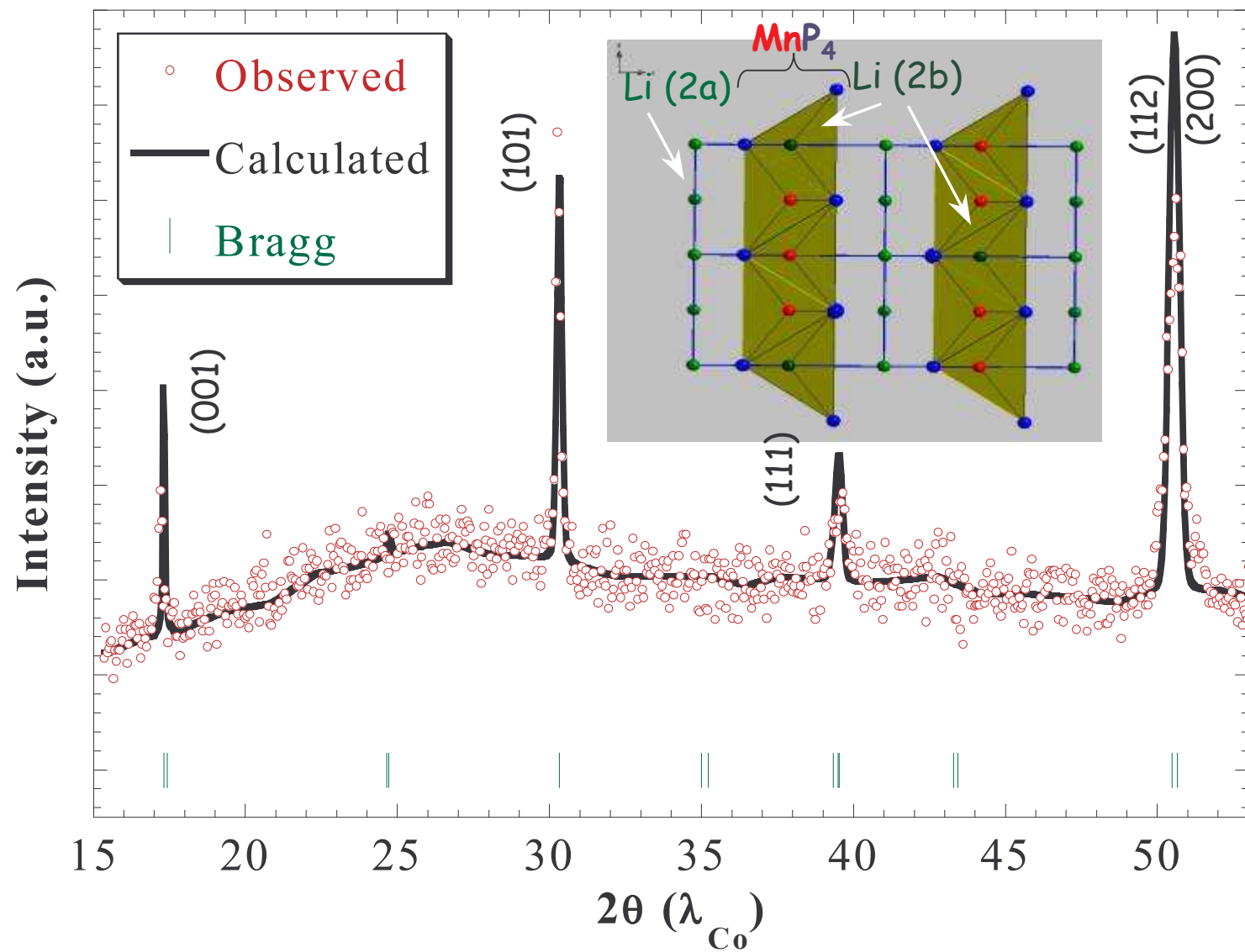


Fig. 2

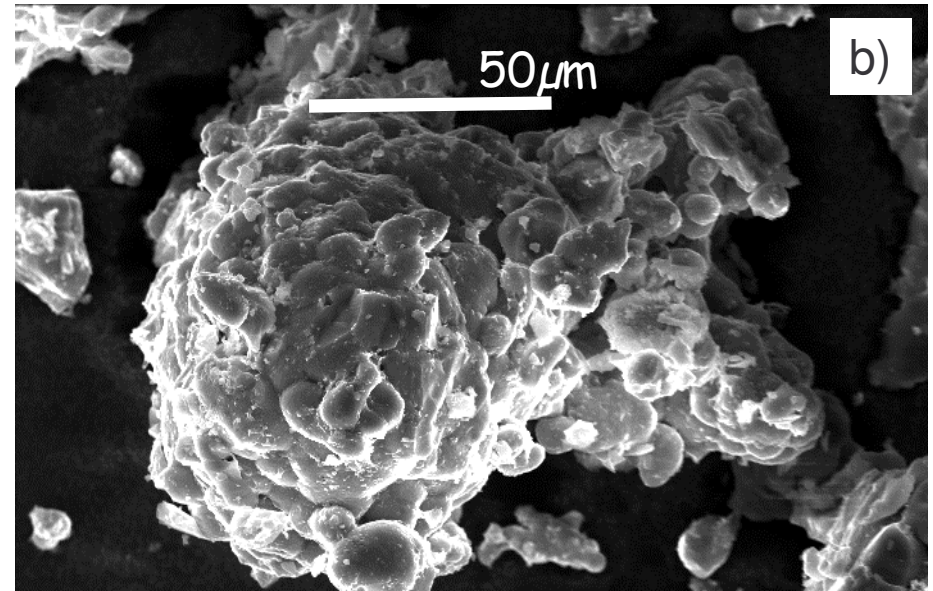
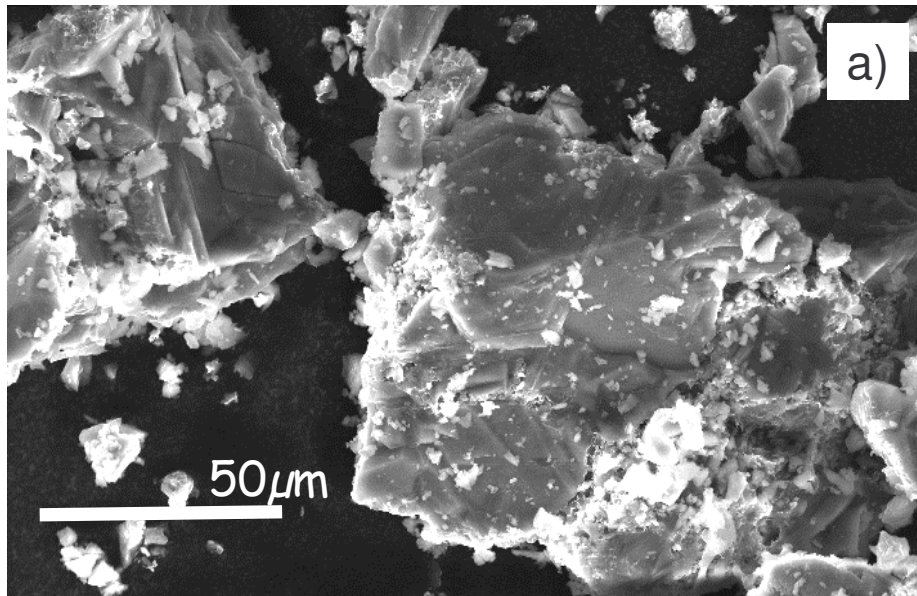


Fig. 3

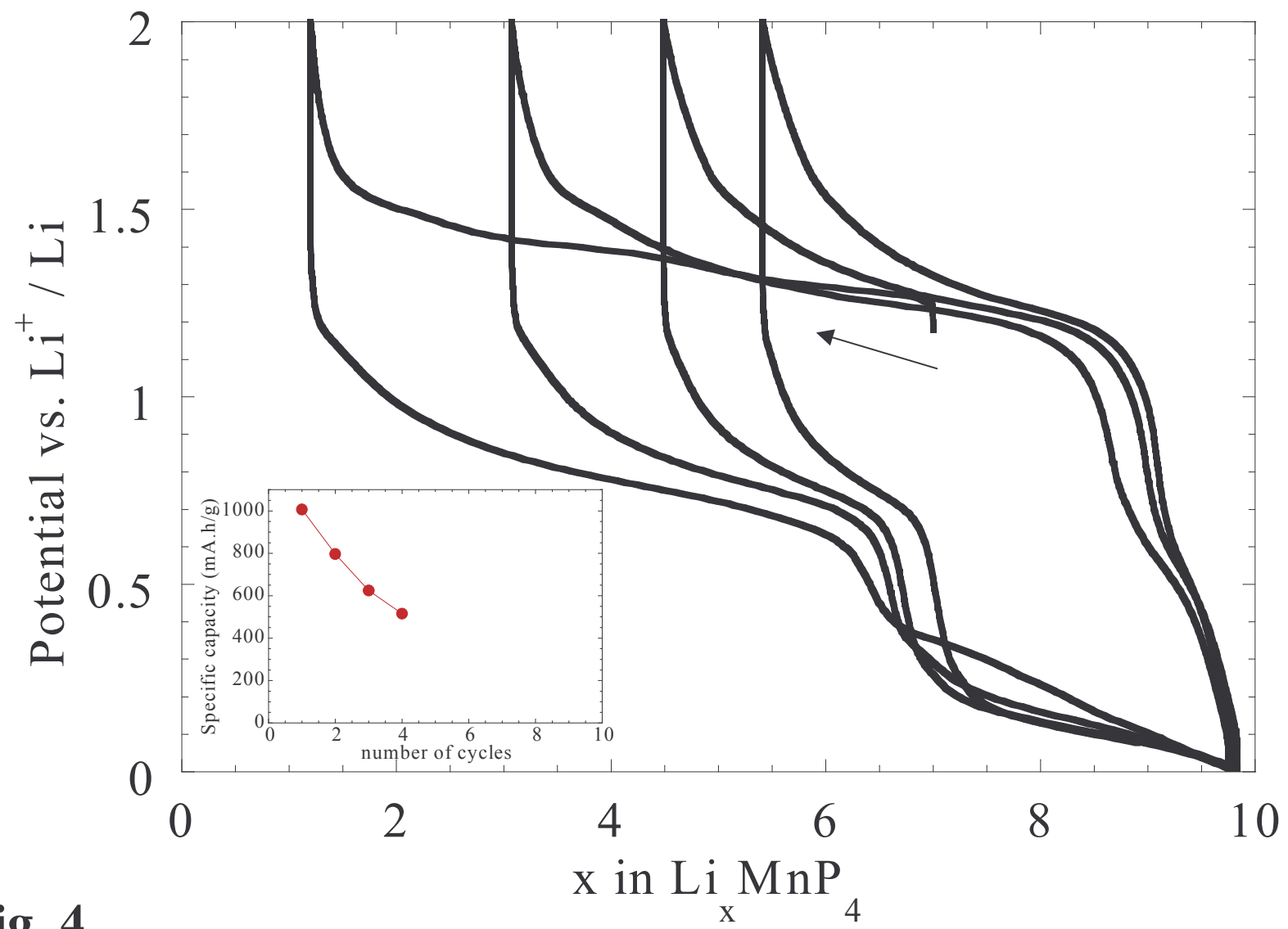


Fig. 4

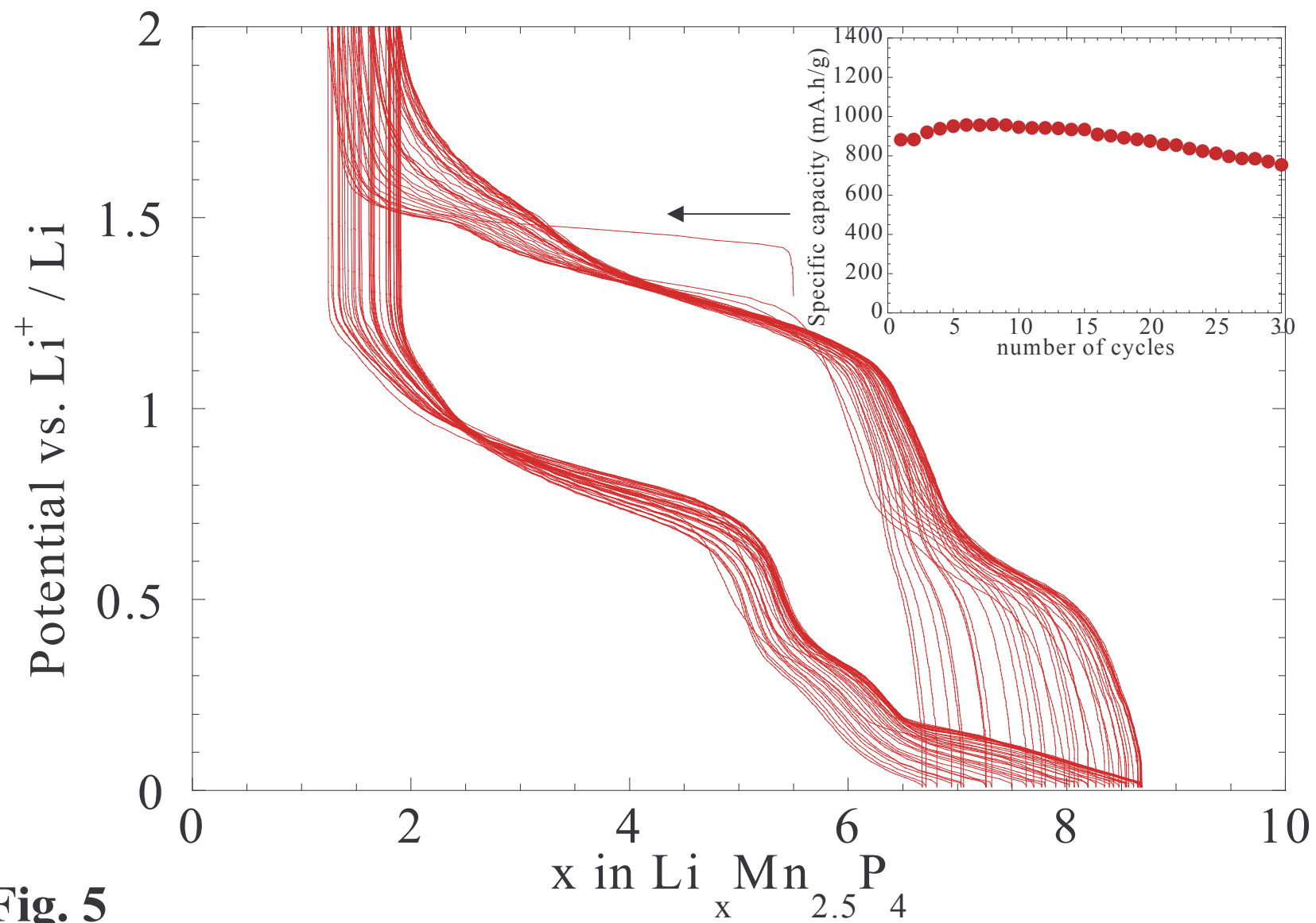


Fig. 5

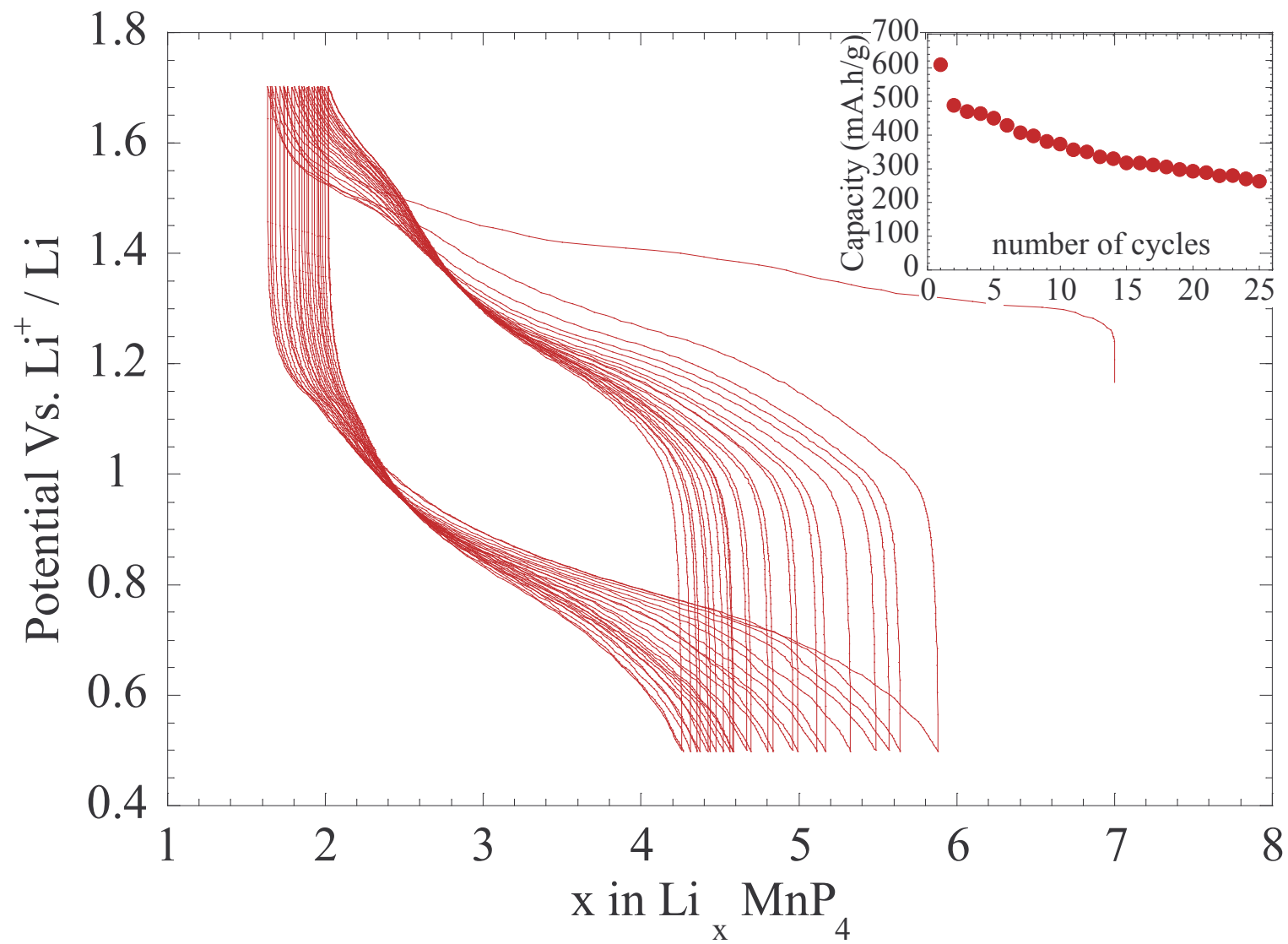


Fig. 6

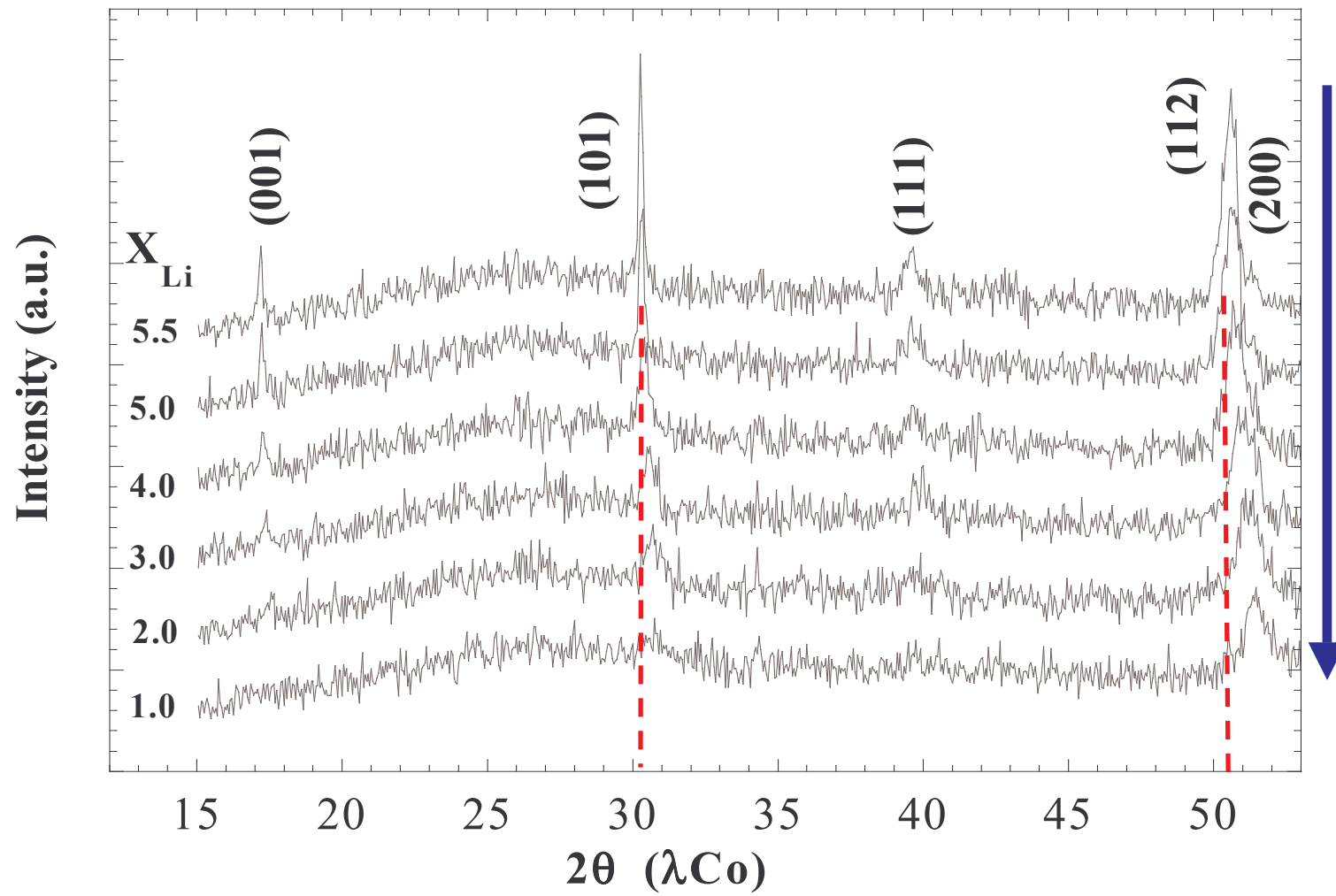


Fig. 7a

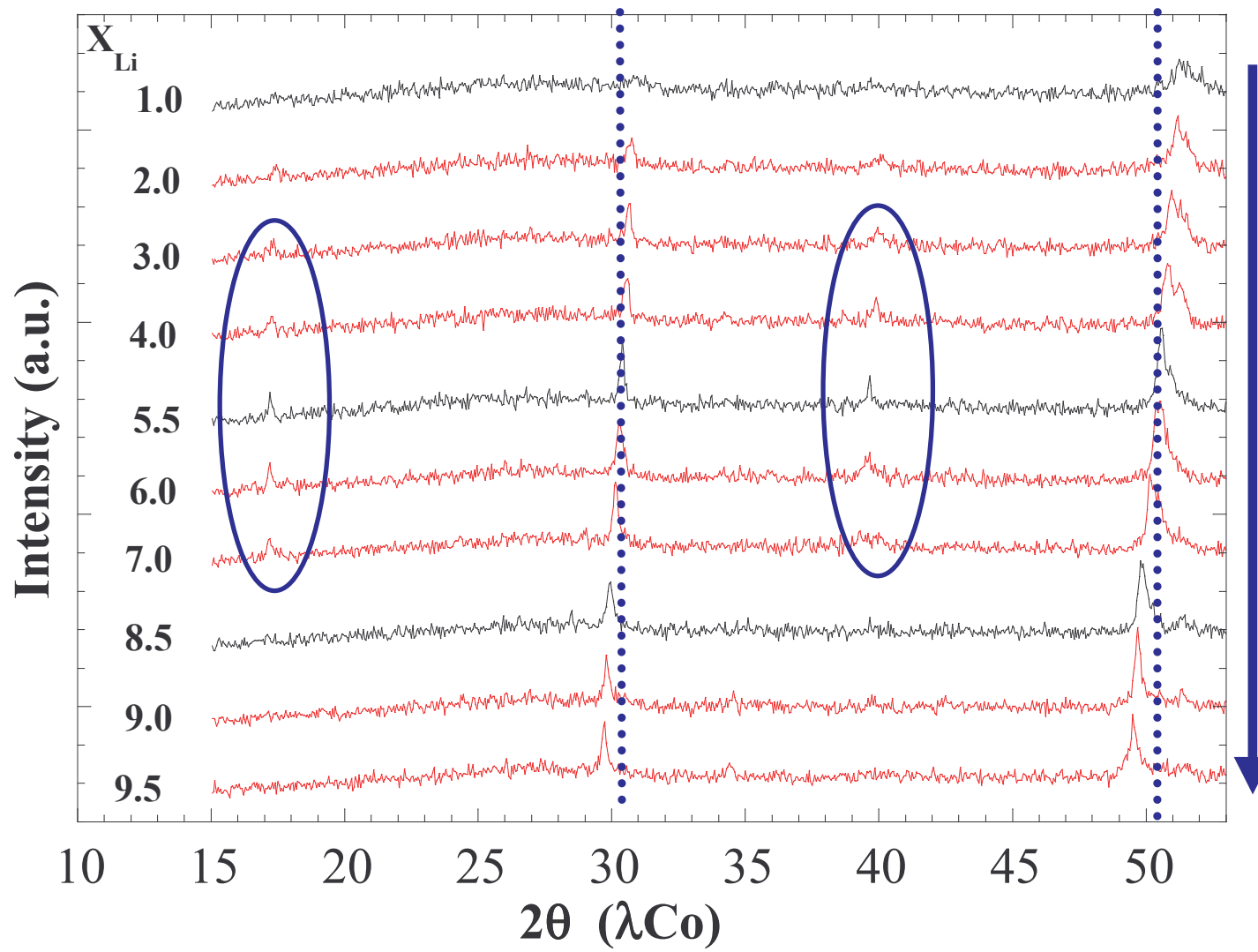


Fig. 7b

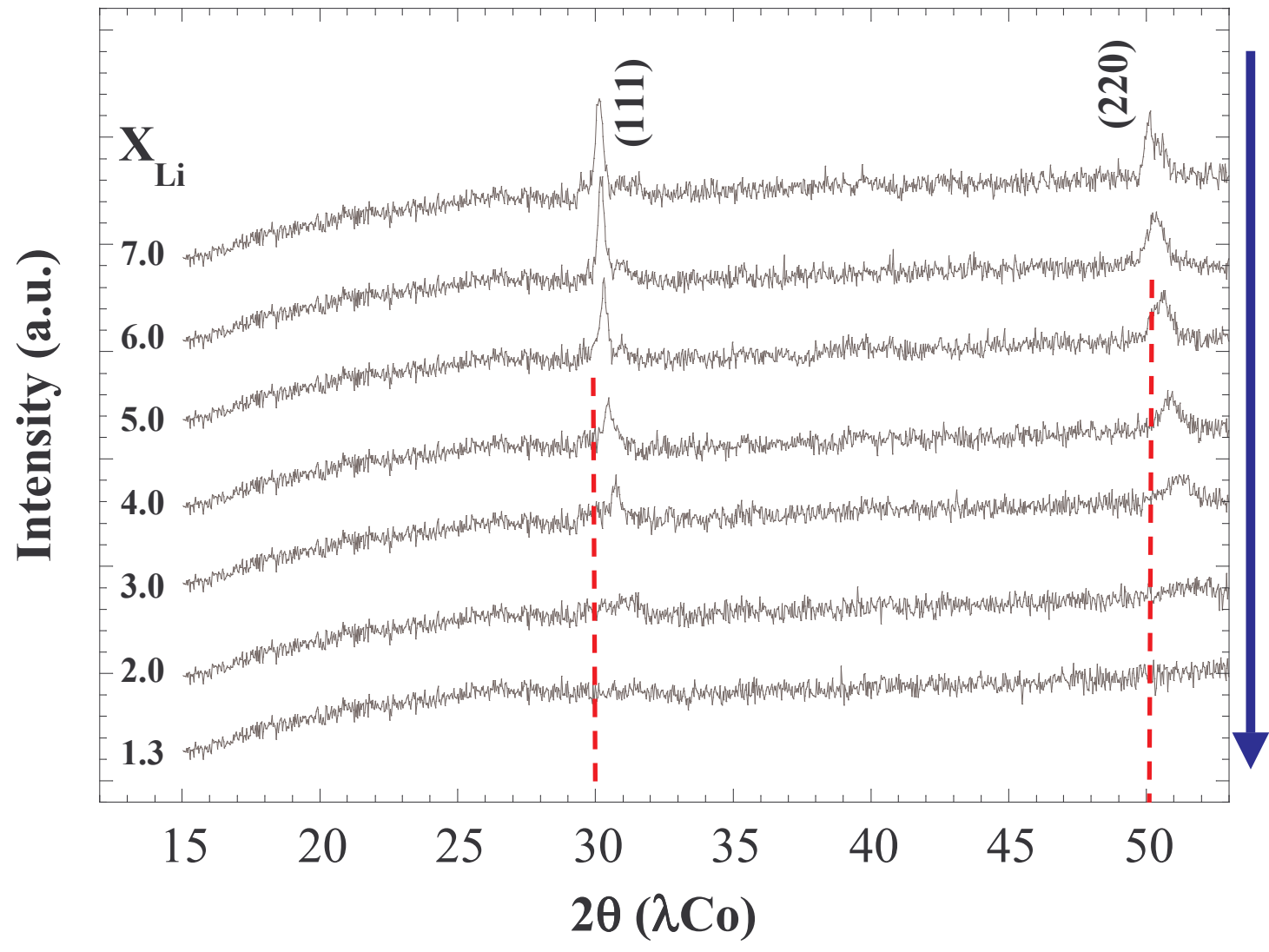


Fig. 8a

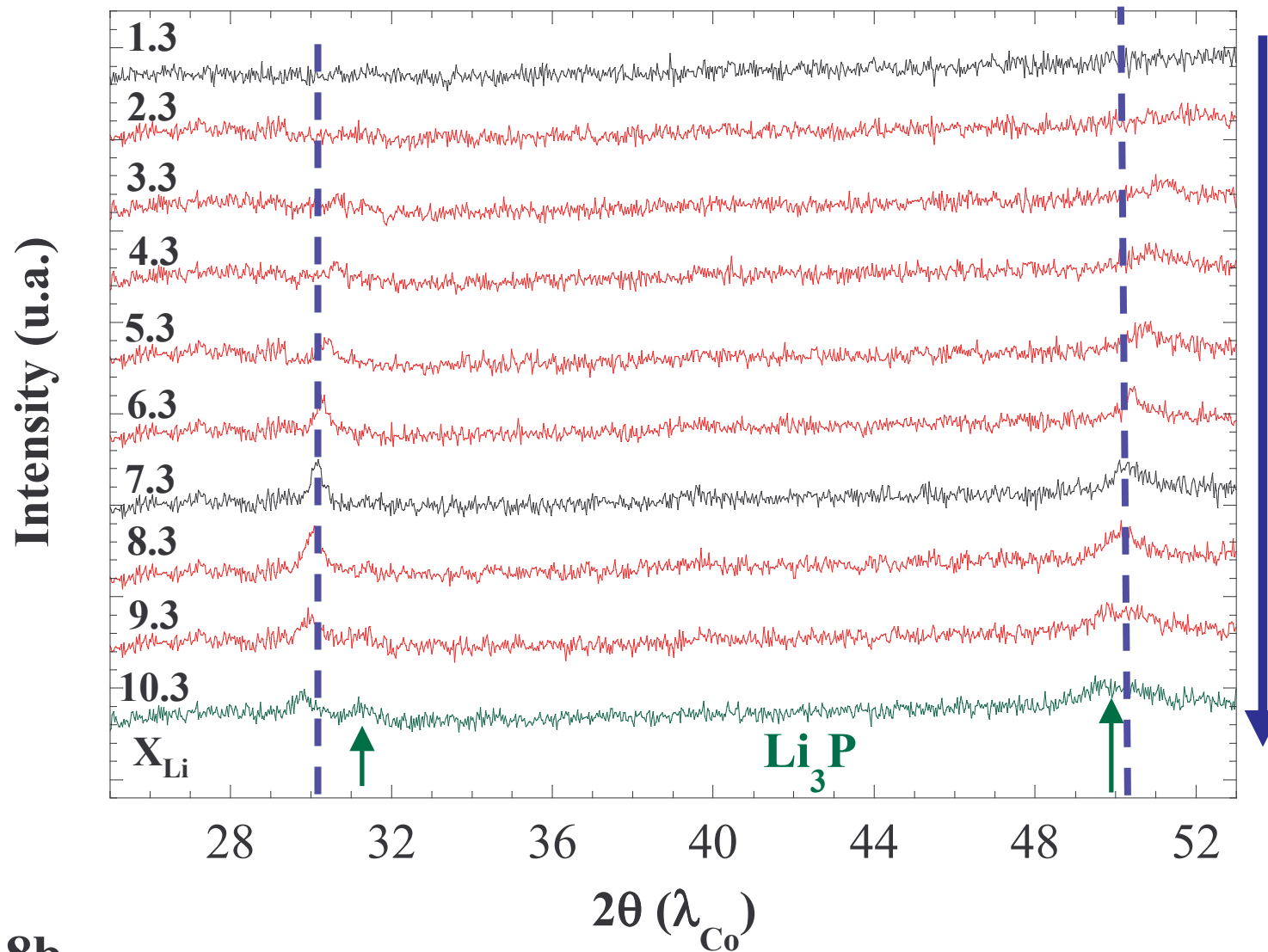


Fig. 8b

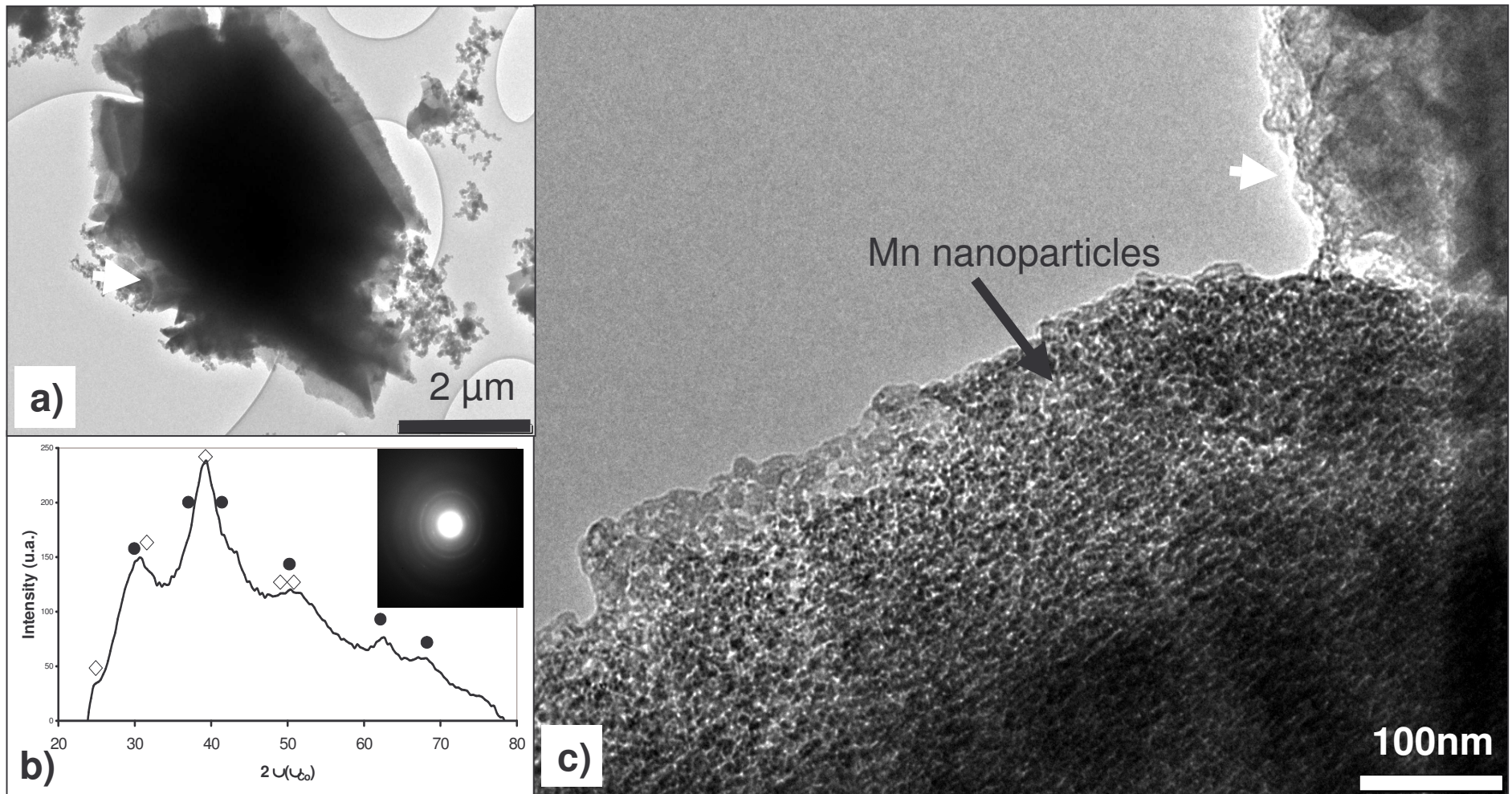


Fig. 9

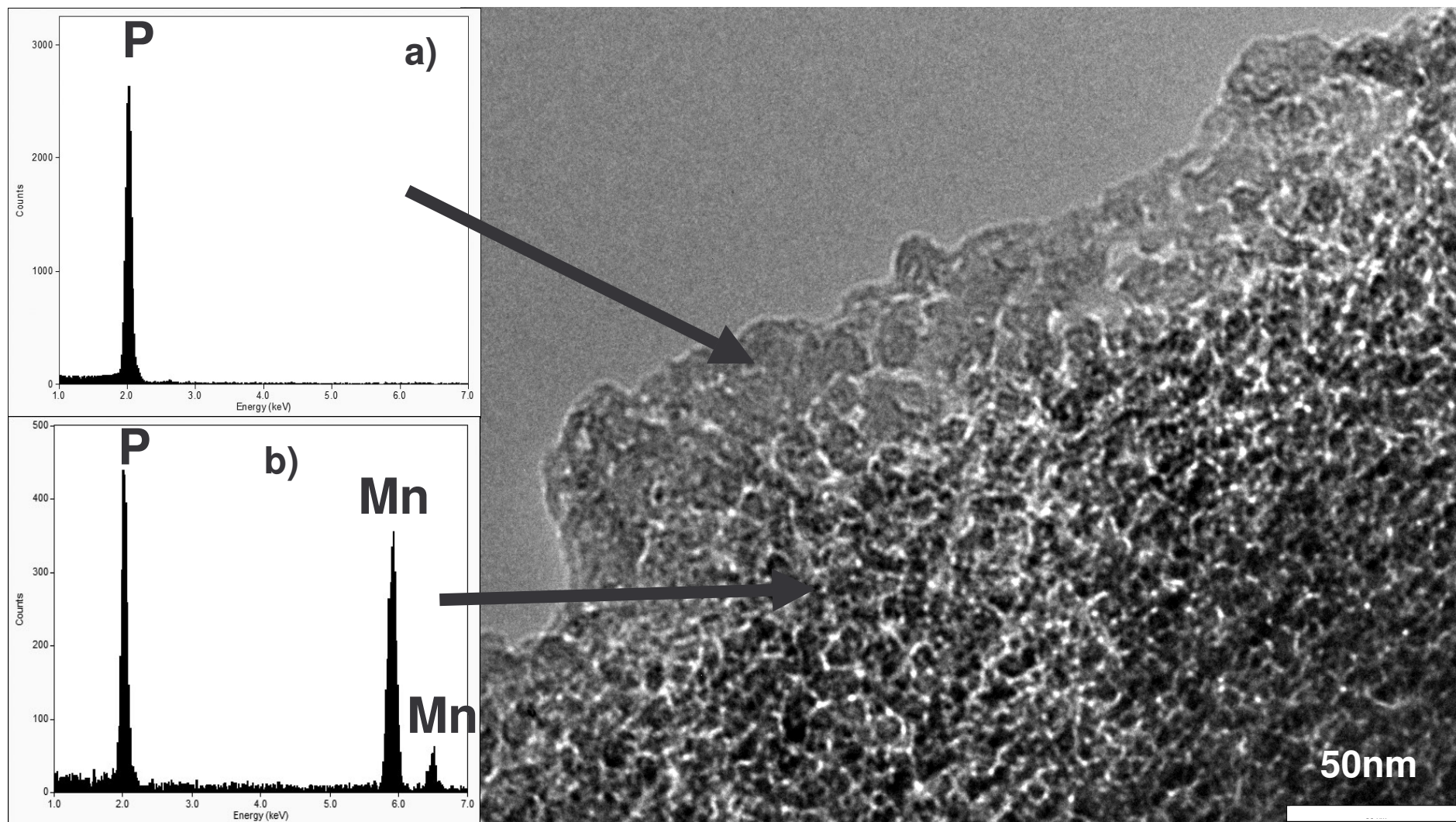


Fig. 10